IJASS
International Journal of
Aeronautical and Space Sciences

ORIGINAL PAPER

Check for updates

Effect of Rotating Inlet Distortion with Multi-distorted Regions on Compressor Stability

Ziwei Wang[1,2] · Zhaolin Fan[1,2] · Fengshun Lu[2] · Jiantao Wang[2] · Shuai Ma[2] · Bin Li[2]

Abstract

The influence of rotating inlet distortion (RID) on compressor stability has attracted widespread attention in academia, mainly about stall margin and onset of rotating stall. However, most of the experiments are conducted on low-speed compressors, most of the simulations are conducted on rotors, and only one distorted region exists at the inlet. This paper aims to explore the influence of RID with more than one distorted region on rotating stall development in the high-speed multi-row compressor. Flow instability of NASA stage 35 under uniform inlet condition and RID with different rotational speeds are simulated. Results indicate that, when rotating stall is fully developed, the RID has little influence on the rotational frequency and number of stall cells, which may be the inherent characteristics of the compressor. However, the onset and the initial state of rotating stall will be primarily influenced. RID with lower rotational speed will delay the occurrence of rotating stall, RID with higher rotational speed will exceed the occurrence of rotating stall but will experience two types of stall states. The causes for these flow phenomena are then discussed in detail. This research's findings can help understand the instability behavior of downstream compressor in multi-spool engine, under the distortion flow induced by upstream compressor.

Keywords Multi-row compressor · Rotating inlet distortion · Multi-distorted regions · Rotating stall

1 Introduction

Aero-engine may encounter inlet distortion problems at many situations, such as changes in maneuvering [1], cross-

Zhaolin Fan, Fengshun Lu, Jiantao Wang, Shuai Ma and Bin Li contributed equally to this work.

✉ Bin Li
45241968@qq.com

Ziwei Wang
ziweigegeya@163.com

Zhaolin Fan
fanz0720@163.com

Fengshun Lu
lufengshun@cardc.cn

Jiantao Wang
wjtao@mail.ustc.edu.cn

Shuai Ma
tuboshu2002@126.com

1 Hypersonic Technology Laboratory, National University of Defense Technology, Changsha 410073, Hunan, China

2 China Aerodynamics Research and Development Center, Mianyang 621000, Sichuan, China

wind [2] and so on. The inlet distortion may lead to aerodynamic instability of compressor, such as rotating stall and so on. As a result, many studies have been done on the analysis of inlet distortion problems, numerically or experimentally.

The paper concentrates on influence of rotating inlet distortion (RID) on development of rotating stall in the compressor. RID can be generated in many situations, for example, in the multi-spool engines, when the upstream compressor is under the situation of rotating stall, the downstream compressor will be imposed by a rotating inlet distortion [3]. RID will affect the stability of compressors, lots of studies have been conducted on this issue.

It was first found by Ludwig et al. [4] in experiments that the stability margin of the compressor is influenced by the rotational speed of the distortion. Longley et al. [3] tested the RID on a low-speed axial compressor, a similar conclusion was reached. Peters et al. [5] tested the influence of RID on a 5-stage high-pressure compressor, and found that the first stall margin degradation peak occurs at a fixed frequency. Nie et al. [6] studied the RID in a low-speed compressor experimentally. They observed that, when the distortion speed is about 50% of rotor speed in terms of co-rotating distortions,

the inlet distortion exhibited a peak in stall margin degradation.

Furthermore, Zhang et al. [7] studied the RID in a low-speed axial compressor, it was found that when the distortion rotates at the propagating speed of the spike-type disturbance, the stall margin is the smallest. Yan et al. [8] observed similar phenomenon in a two-stage low-speed compressor, but the stall inception is modal-type. Zhang and Hou [9] studied the RID in a single-stage low-speed compressor. For co-rotating inlet distortion, there existed a peak in the stall margin. They concluded that the stall inception is triggered by the RID through the long length scale disturbances. Li et al. [1] studied the RID in a two-stage low-speed compressor, there existed two peaks in the stall margin for different rotational speeds of RID. It was concluded that the first peak is associated with an initial stall inception, the second peak is related to a spike-type inception. Zhang et al. [10] studied the influence of inlet distortion on stall margin of NASA rotor 67. Different rotational speeds of rotor 67 is studied, it is found that when the corrected speed decreases, the stall margin of the rotor decreases.

Although great progress has been made, the mechanism of how the rotating stall is influenced by RID has not been revealed. Most of the experiments are conducted on low-speed compressors. However, the influence of RID on high-speed compressors should also be studied in depth. Most of the studies focus on the influence of RID on stall margin or stall inception. However, the whole development process of the rotating stall should be studied to further reveal the mechanism of how RID influences the development of rotating stall in the compressor.

What is more, the RID used in the previous studies was simple, which may not completely simulate the real configuration of the upstream stall cell. The distortion generator was limited to generating a single-cell configuration with a fixed circumferential extent [8]. For multi-spool engines, when the upstream compressor is under the situation of rotating stall, the downstream compressor will be imposed by a rotating inlet distortion with more than one region. The RID with more than one distorted region should also be studied.

In this paper, the influence of RID with more than one distorted region on development of rotating stall in a high-speed multi-row compressor is studied. The full-annulus unsteady RANS simulation is conducted. The paper focuses on the development of stall cells under multiple distortion regions, rather than the influence of the number of distortion regions on the development of stall cells. Therefore, the number of distortion regions is selected as 4.It is found in previous studies that the co-rotating distortion has a larger negative effect than counter-rotating distortion [1, 2], so the study in this paper concentrates on the co-rotating distortion.

Taking the results under uniform inlet as the control group, the stall development simulation under co-rotating distur-

bance with different rotational speeds is carried out, which are 0%, 50% and 100% design rotational speed, respectively. Strictly speaking, 0% design rotational speed is not "rotating" inlet distortion, but it can be used as a bridge to compare the results between RID and uniform inlet. The paper is organized as follows:

1. Validate the simulation strategy for rotating stall by comparing results with the experimental data [11–13] and the former simulation study [14, 15].
2. Compare the differences among compressor stall flow under uniform inlet condition and RID with different rotational speeds.
3. Study the flow phenomena discovered through analysis of flow field variable pulsation and flow field structure.

2 Flow Solver and Simulation Strategy

2.1 Flow Solver

The in-house software ASPAC [16] is used in the current research. The 3-D compressible Navier–Stokes equations are solved by a fully-implicit scheme with a cell-centered finite volume method. The inviscid flux is evaluated by Roe Scheme with the Van Albada limiter. The viscous flux is determined in a central differencing manner with Gauss's theorem. The second-order backward difference is applied to the temporal derivative and the inner iteration is conducted at each time step. The current computations use the one-equation Spalart–Allmaras turbulence model. The parallel is conducted based on MPI.

2.2 Simulation Settings

The transonic single-stage compressor NASA stage 35 [11] is chosen as the test case.

2.2.1 Computation Domain and Boundary Conditions

The numerical model of Stage 35 is shown in Fig. 1.

192 ARM V64 CPU cores are used to conduct full-annulus simulation. A temporal discretization level of 1656 physical time steps per rotor revolution and 50 inner iteration steps is used. The rotational speed is 17188.7rpm, the inlet total pressure is 101325Pa, and the inlet total temperature is 288.15K. The static pressure at hub of the outlet is gradually increased to simulate the speedline.
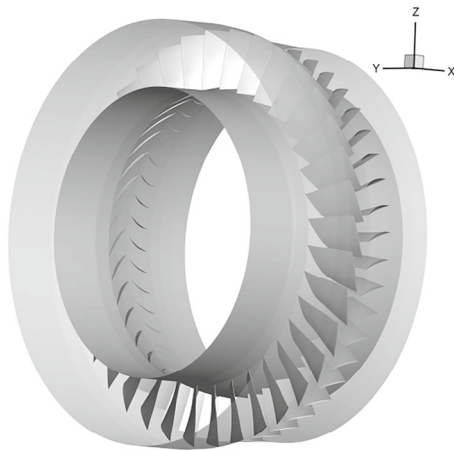
Fig. 1 Numerical model of NASA stage 35

Table 1 Comparison of performance parameters with different cell numbers (steady)

Grid	Cell number	Relative total pressure ratio (%)	Relative total temperature ratio (%)
A	1.08e6	100	100
B	4.75e5	99.86	100.02
C	3.90e5	99.82	100.06

Table 2 Comparison of performance parameters with different cell numbers(full annulus unsteady)

Grid	Cell number	Relative total pressure ratio (%)	Relative total temperature ratio (%)
A	4.41e7	100	100
B	1.92e7	99.88	100.02
C	1.59e7	99.82	100.06

2.2.2 Grid Independence Test

The grid of the compressor is shown in Fig. 2. Using the same grid topology (Fig. 2a), the grid quality is guaranteed to be consistent with the changing of grid cells number on the topology. All grids are refined near the boundary layer, with the height of the first layer of the grid is $3e^{-6}m$ and y^+ is about 1. Grid independence test using the same boundary conditions was conducted. The results of steady simulation (mixing plane method) with single passage grid are shown in Table 1. The results of the full annulus unsteady simulation with full annulus grid are shown in Table 2. The total temperature ratio and total pressure ratio change little with the increase of cell number and the error is less than 1%, which meets grid independence testing requirements.

Based on the above factors, the "Grid B" is selected as the computational grid. The grid details are shown in Fig. 2b, c.

2.2.3 Time Step Independence Test

The time step independence test for unsteady simulation is conducted using the same boundary conditions and the initial flow field. Different temporal discretization levels per rotor revolution are tested.
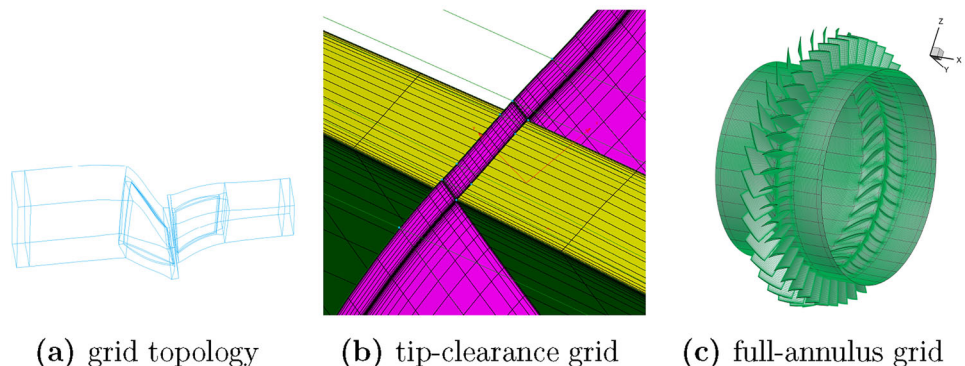
The variations of total temperature ratio and total pressure ratio converge when the temporal discretization level is bigger than 1300 steps per rotor revolution, as shown in Fig. 3. The temporal discretization level of 1656 steps per revolution is chosen when conducting full annulus simulation.
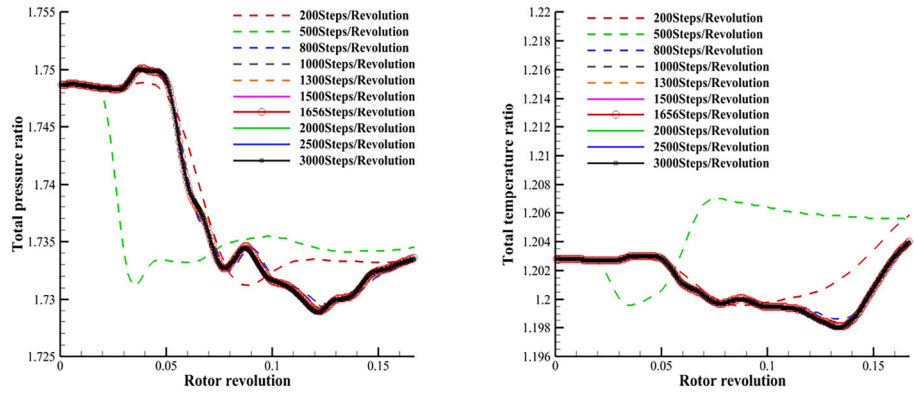
2.2.4 Case Description

The speedline of Stage 35 at design speed 17188.7rpm is calculated based on full-annulus simulation [16], which is then compared to results of software TURBO [17] and Experiment [12], as shown in Fig. 4.

The unsteady flow field at near stall point is used as the initial flow field. The near stall point is marked in Fig. 4, based on which the rotating stall development for cases with uniform inlet condition or RID is calculated, which mim-
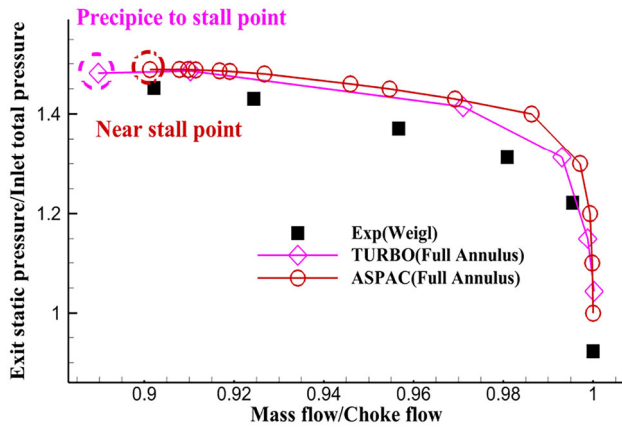
Fig. 2 Grid of NASA stage 35

(a) grid topology **(b)** tip-clearance grid **(c)** full-annulus grid

Fig. 3 Variations of performance parameters with different temporal discretization levels

(a) total pressure ratio **(b)** total temperature ratio

Fig. 4 Speedline of Stage 35

Table 3 Description of four cases

Case	Description
Case1: UNI	Uniform inlet condition
Case2: CO-0.0 RID	Rotating inlet distortion, 0% design speed
Case3: CO-0.5 RID	Rotating inlet distortion, 50% design speed
Case4: CO-1.0 RID	Rotating inlet distortion, 100% design speed

Fig. 5 Total pressure distribution of RID at the inlet

ics the sudden occurrence of flow distortion. Four cases are designed, listed in Table 3.

In terms of Case1, the inlet total pressure is 101325Pa. For the cases with RID, referring to the calculation and experiments of other researchers [18], the inlet total pressure distortion in the form of the sine wave is designed as Eq. (1). In this paper, the RID of different cases has different rotational speeds.

$$P_{\text{total}}(\theta) = 101{,}325\,\text{Pa} + 101{,}325\,\text{Pa}$$
$$\cdot 0.1 \cdot \sin(4 \cdot (\theta + (\omega_{\text{rotor}} - \omega_{\text{RID}}) \cdot t)), \quad (1)$$
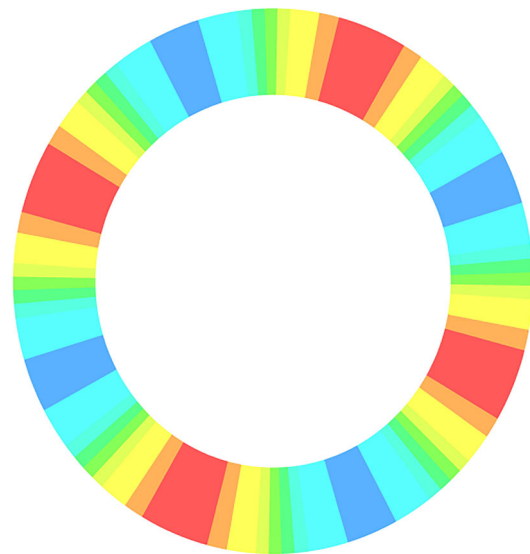
where θ is the circumferential position of grid cell center at the inlet boundary when $t = 0$ (corresponding to the physical time of initial flow field). The total pressure distribution of RID at the inlet at a time is shown in Fig. 5. ω_{RID} of different cases is listed in Table 3.

There are 4 distortion regions circumferentially, to mimic distortion induced by the upstream compressor. When simulating the four cases, the inlet total temperature is 288.15 K, the inlet total pressure is expressed as Eq. (1). At the outlet, the "choked" throttle model is applied, which allows variation of exit static pressure to match the compressor exit mass flow. The formula is expressed as Eq. (2).

$$P_{\text{outlet}} = P_{\text{environment}} + \dot{m}_r^2/k_t, \quad (2)$$

where P_{outlet} is static pressure at the hub of the outlet, the radial equilibrium is then applied at outlet. $P_{\text{environment}}$ is the environment pressure which is set as 101,325 Pa, $\dot{m}_r$ is mass flow at outlet, k_t is a parameter to control the throttle area. In terms of the throttle model, when mass flow is equal, the smaller k_t is, the larger $\delta P = P_{\text{outlet}} - P_{\text{environment}}$ is, which means the throttle valve is further turned down.

2.2.5 Validation of Simulation Results of Rotating Stall

NASA stage 35 has been studied by several research groups as a basic model for rotating stall research.

In the early days, due to the limitation of computing resources, most simulation studies were based on single blade passage or multi-blade passages.

Chen et al. [14] was the first to use the full-annulus grid to simulate the rotating stall in NASA stage 35. In their simulation, the tip clearance is modeled. It is found that the speed of modal disturbance is 84% rotor speed, which consists of multiple stall cells. After that, some spike disturbances emerge, and the rotational speed of which gradually slow down. Finally, a single rotating stall cell of 43% rotor speed is formed.

In the research of Gan et al. [15], the tip clearance is gridded. It is found that the stall disturbance transports to more blade passage with about 90% rotor speed. Then one stall cells propagate at 50% of the rotor speed.

Bright et al. [13] conducted the stability experiment of NASA stage 35 under the uniform inlet condition. However, it is pointed by Chen et al. [14] that there are no pressure trace data available at design speed. Therefore, they use the 85% speed case to compare with the simulated results. The same experiment results are also used to verify the numerical results in this paper.

In Bright's experiment, a continuous throttling maneuver is used to transition the compressor into stall. In Chen's simulation, the throttle condition is changed in discrete steps. In Gan's simulation, the outlet condition during the stalled process is not mentioned. In the current simulation, a continuous throttling behavior is applied.

The sampling points are placed in the relative coordinate system, an example is shown in Fig. 6. The sampling frequency is 1656 times per revolution. The near stall point in Fig. 4 is taken as $t = 0$.

Based on Eq. (3), the sampling results in the relative coordinate system can be converted into the results in the absolute coordinate system:
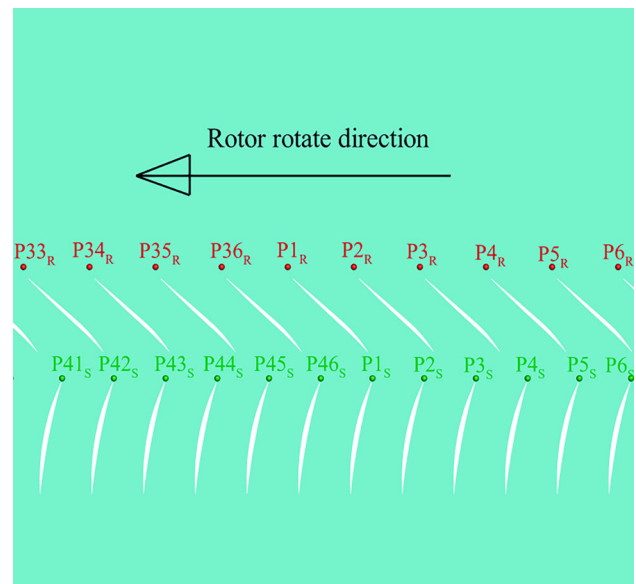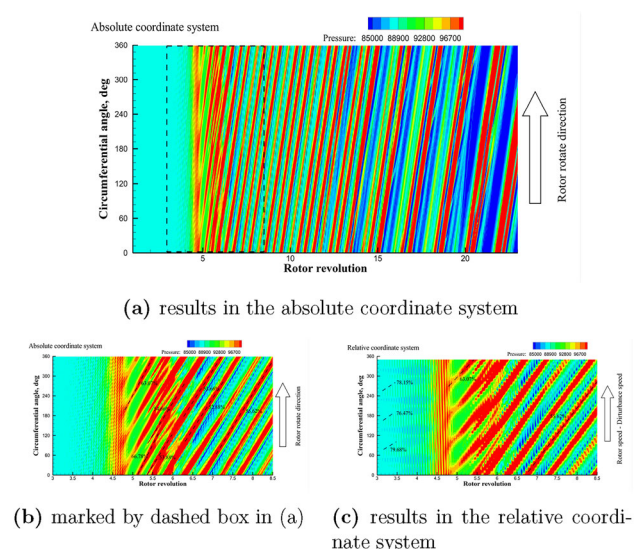

Fig. 6 An example of the sampling points

(a) results in the absolute coordinate system

(b) marked by dashed box in (a)   **(c)** results in the relative coordinate system

Fig. 7 Results of ASPAC (sampling points across tip span in front of blade leading edge)

$$Q_{\text{Relative}}(x, r, \theta, t) = Q_{\text{Absolute}}(x, r, \theta + \omega_{\text{coordinate}} \cdot t, t). \tag{3}$$

Collect and process the pressure trace data at the same relative position of each blade passage in the circumferential direction, the pressure variations at different circumferential positions in the absolute coordinate system and the relative coordinate system can be obtained, as shown in Fig. 7. The stall inception disturbance transports circumferentially with about 78% rotor speed, then gradually forms a single rotating stall cell of 55.62% rotor speed.
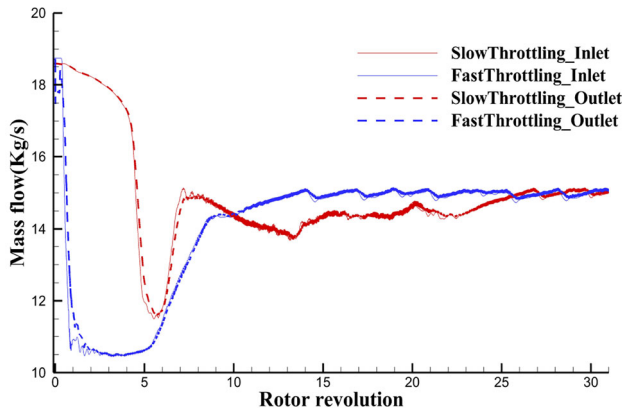
Fig. 8 Variations in mass flow with slow throttling behavior and fast throttling behavior

To accelerate the formation of the stall cells, a fast throttling behavior is also applied. The comparison of mass flow variations with continuous throttling behavior (slow throttling) and fast throttling behavior is shown in Fig. 8. For the continuous throttling behavior, the throttle valve is closed in 10 rotor revolutions. For the fast throttling behavior, the throttled is closed in 0.01 rotor revolutions.

The pressure trace results of sampling points at the blade tip are compared in Fig. 9.

When applying the fast throttling behavior, the pre-stall phenomenon is not well captured, but the post-stall phenomenon is well captured. Moreover, the fast throttling behavior can be used to quickly induce stall and facilitate stall development analysis. The four cases mentioned in Table 3 will be simulated with fast throttling behavior.

3 Result Analysis

The same throttle process is applied to the four cases. The time history of mass flow at the inlet and outlet for the

four cases are shown in Fig. 10. After the throttle model is imposed, the mass flow of 4 cases is throttled to low mass flow situation. The mass flow increases gradually and then fluctuates near the mass flow of the fully developed rotating stall. The order of the time required for the four cases to enter the rotating stall state is CO-1.0 RID < CO-0.5 RID < UNI < CO-0.0 RID.

The pressure of the sampling points is normalized as Eq. (4), to avoid pressure traces of different passages overlapping each other in Fig. 11.

$$P = \frac{P - 100,000}{2000}. \tag{4}$$

It is found the rotating stall occurs in the CO-0.0 RID case later than that in the UNI case. However, the flow in the CO-0.5 RID case and CO-1.0 RID case enters into the rotating stall state much earlier than that in the UNI case. Meanwhile, the flow in CO-0.5 RID case and CO-1.0 RID has experienced two stall states, as illustrated in Fig. 11, with the blue line representing stall state 1 and the red line representing stall state 2. It indicates that, for the current test case, the RID with lower co-rotational speed will delay the occurrence of the rotating stall, and the RID with higher co-rotational speed will exceed the occurrence of rotating stall but will experience two types of stall states. The ratio of the angular velocity of disturbance to that of the rotor is roughly calculated. The results of the four cases are illustrated in Fig. 11.

The spatial frequency transform (SFT) analysis of the 36 sampling points is conducted. The 1st-order harmonic result of SFT is shown in Fig. 12. The amplitude of 1st harmonic is relatively small before the emergence of stall disturbance, which increases gradually with the development of rotating stall and then fluctuates near the max value. For the UNI case and the CO-0.0 RID case, the increasing process of the first harmonic amplitude corresponds to the strengthening process

(a) slow throttling behavior   **(b)** fast throttling behavior
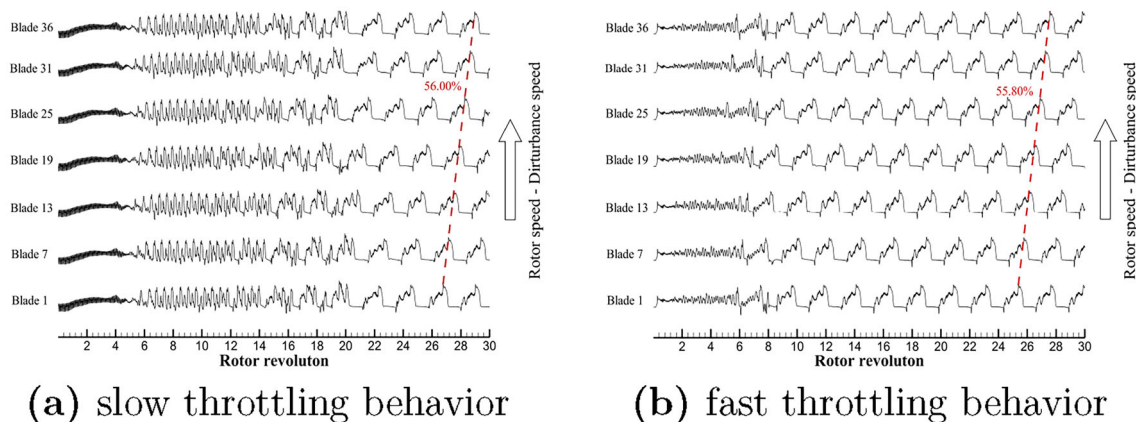
Fig. 9 Variations in pressure at blade tip (relative coordinate system)
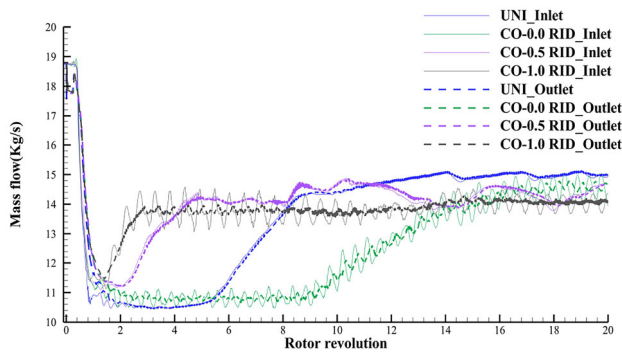
Fig. 10 Variation of mass flow

of stall disturbance. For the CO-0.5 RID case and the CO-1.0 RID case, the growth process of the first harmonic amplitude corresponds to the development process of stall state 1. After entering the final state, the amplitude of the first harmonic is stabilized.

The wavelet transform (WT) analysis of pressure signals of the sampling points in the first rotor passage is shown in Fig. 13. Besides, the fast fourier transform (FFT) analysis

is also conducted, which is used to accurately locate the frequency extremum in WT analysis. The stall cell is of 45.16% rotor frequency when the rotating stall is fully developed. In the absolute coordinate frame, it is $1 - 0.4516 = 0.5484$ times of rotor frequency, similar to the results generated from Fig. 11, which indicates the RID has little influence on the rotational frequency of stall cells when the rotating stall is fully developed, consistent with the previous studies [19].

Besides, some flow phenomena need to be further explored, which are listed as follows:

1. Why the CO-0.0 RID delays the occurrence of the rotating stall, but the CO-0.5 RID and CO-1.0 RID will exceed the occurrence of the rotating stall?
2. In terms of the CO-0.5 RID case and CO-1.0 RID case, what are the corresponding flow structures in different states, such as before pre-stall state, stall state 1, stall state 2, and so on?
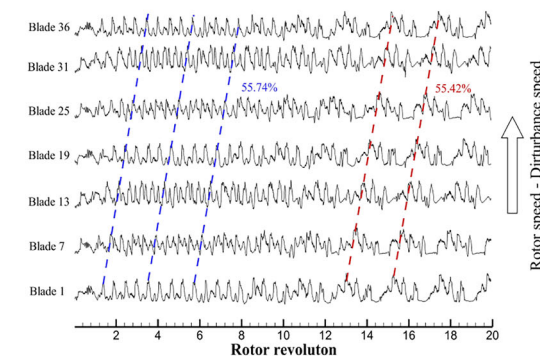3. What drives the transition from stall state 1 to stall state 2?
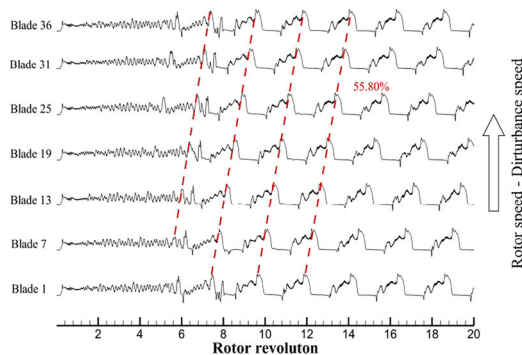
(a) UNI
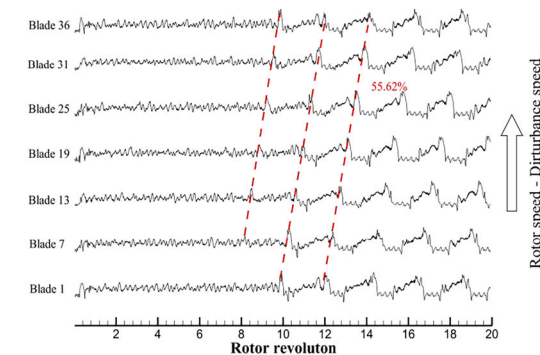
(b) CO-0.0 RID
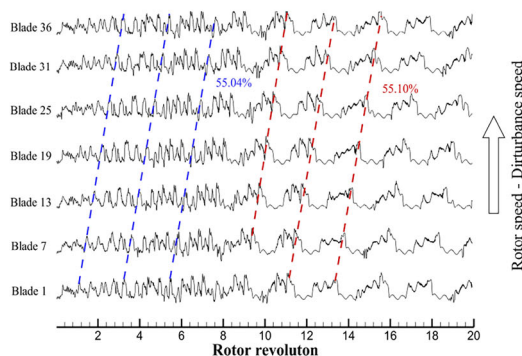
(c) CO-0.5 RID

(d) CO-1.0 RID

Fig. 11 Time traces of wall pressure measured at blade tip

(a) UNI

(b) CO-0.0 RID
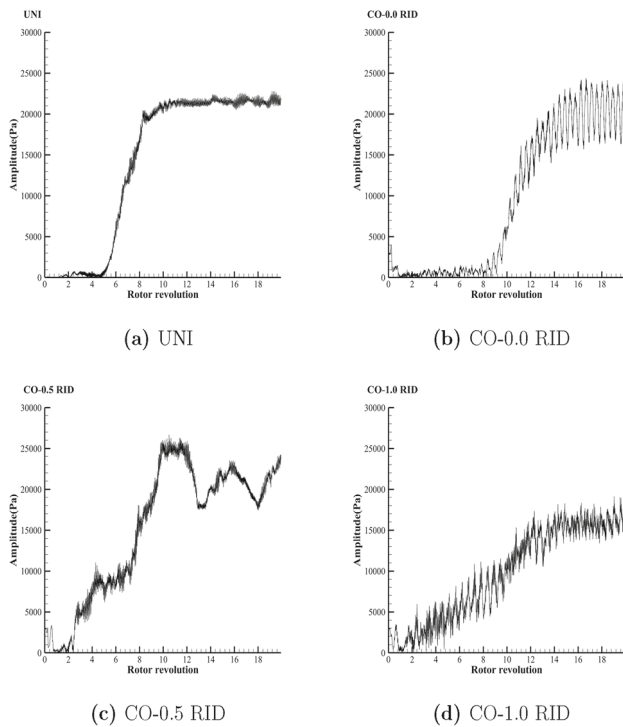
(c) CO-0.5 RID

(d) CO-1.0 RID

Fig. 12 First-order harmonic of spatial frequency transform

4 Discussion

4.1 Variations in Flow Field Across Tip Span

To better observe the stall development process under the four cases, the flow field near the tip span at different times is generated, as shown in Fig. 14.

The entropy distributions at 98% span of 4 cases at different times are illustrated in Fig. 14. To show the flow field more clearly, the axial coordinate is magnified four times. The entropy is calculated as Eq. (5).

$$
\begin{aligned}
\text{Entropy} &= C_{\text{v}} \ln \frac{(P/P_{\text{ref}})}{(\rho/\rho_{\text{ref}})^{\gamma}} \\
P_{\text{ref}} &= 101{,}325\,\text{Pa} \\
\rho_{\text{ref}} &= 1.22505\,\text{kg/m}^3,
\end{aligned}
\tag{5}
$$

where C_{v} is constant volume specific heat and γ is the specific heat ratio.

When the throttle is fast closed, the mass flow has decreased to the lowest value in the 4 cases, the flow is blocked, as shown in the pictures at bottom of Fig. 14. In the UNI case and CO-0.0 RID case, with the increase of mass flow, some blade passages exit from the blocked state. After the mass flow stabilizes around the mass flow of rotating stall status, the stall cells are formed and keep nearly unchanged with time. In the CO-0.5 case and CO-1.0 case, with the increase of mass flow, four stall groups emerge, which is denoted as stall state 1. It can be got from Fig. 13c,
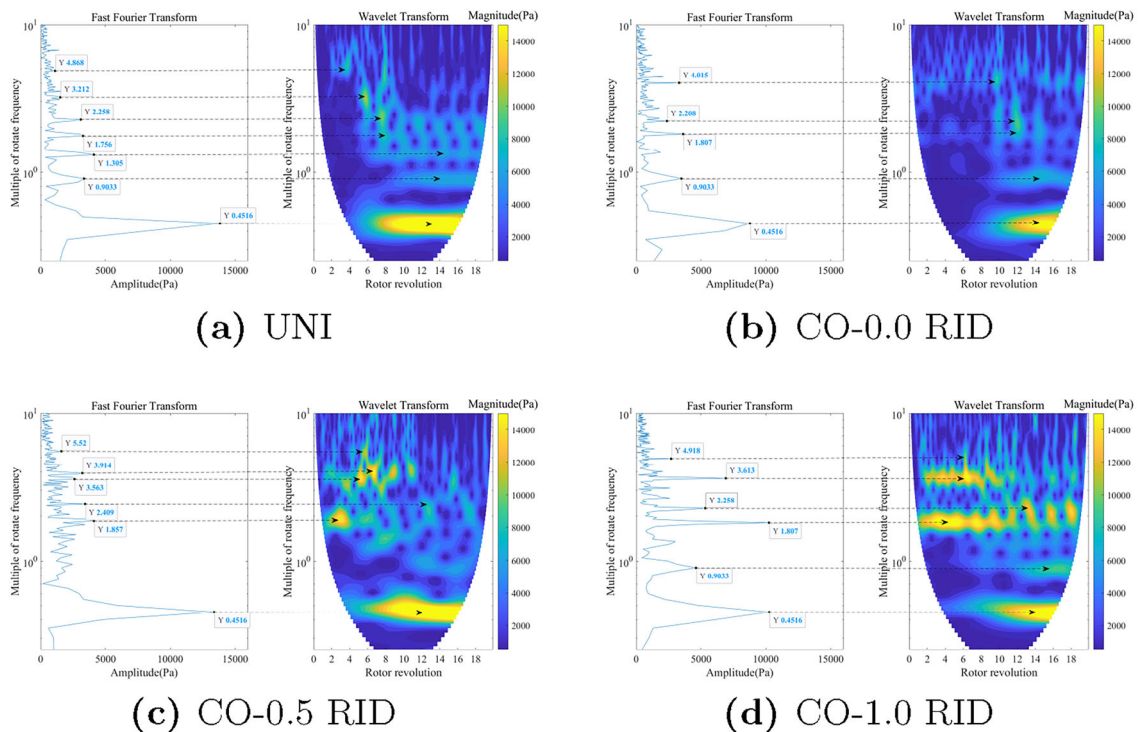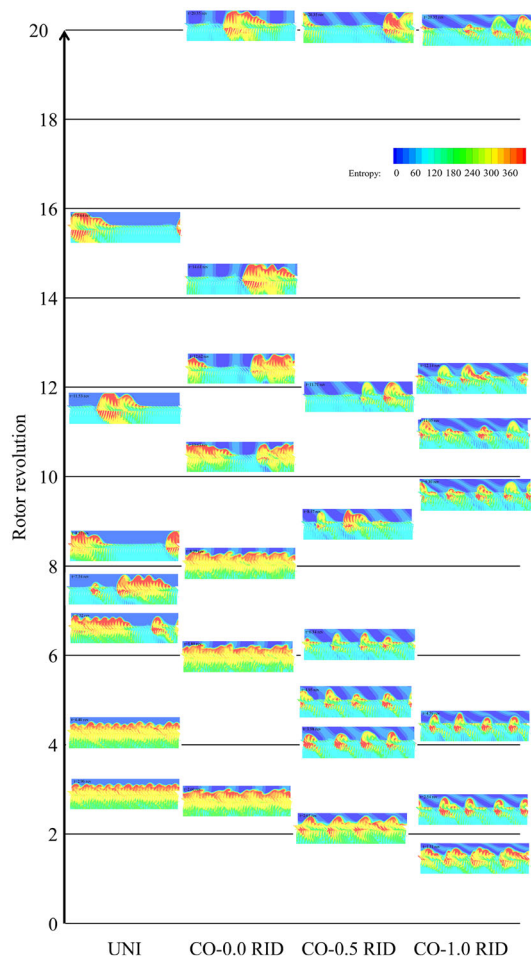

(a) UNI

(b) CO-0.0 RID

(c) CO-0.5 RID

(d) CO-1.0 RID

Fig. 13 FFT analysis and WT analysis of pressure variations of sampling point near shroud of first rotor passage

Fig. 14 Entropy distribution at 98% span

d that the rotational frequency of the stall groups are 1.857 and 1.807 times of rotor frequency, respectively. As there are four groups in the annulus, the actual rotational frequency for the two cases are 1.857/4 = 0.46425 and 1.807/4 = 0.45175 times of rotor frequency, which are close to the rotational frequency of the stall cells when it is fully developed. After that, the number of stall groups gradually decreases, and finally only one stall group exists, which is denoted as stall state 2. It indicates that stall state 1 is not stable, which will eventually be transformed into stall state 2. The transition process appears earlier in the CO-0.5 case than in the CO-1.0 case.

4.2 Effect of Inlet Distortion on Pre-Stall Flow Field

The RID cases are chosen for comparison, with the initial flow field at near stall condition chosen as the control group. The flow field at 98% span for the control group is listed in Fig. 15a. The flow field for the CO-0.0 case, CO-0.5 case, and CO-1.0 case when the mass flow is close to the lowest value are listed in Fig. 15b–d.

In Fig. 15, P_t denotes the total pressure, MassFlow$_x$ denotes the axial mass flow, and Kinetic Energy$_x$ denotes the axial kinetic energy, which is calculated as Eq. (6).

$$\text{Mass Flow}_x = \rho \cdot Ma_x$$
$$\text{Kinetic Energy}_x = \frac{1}{2}\rho \cdot Ma_x{}^2. \tag{6}$$

It can be seen from the inlet regions of Fig. 15b–d that, for flow in the distorted regions with higher total pressure, the axial mass flow and axial kinetic energy are usually larger than that in the distorted regions with lower total pressure.

As can be seen from Fig. 16, after the outlet is throttled, the mass flow is blocked. For the RID cases, under the influence of 4 distorted regions, 4 protrusions between the inlet and the leading edge of rotor blades are formed, corresponding to 4 distorted regions. Compared to CO-0.0 RID, the rotational speeds of inlet distortion in CO-0.5 RID and CO-1.0 RID are closer to the rotor speed, and have a more significant impact on the rotor blade channel, forming 4 more obvious protrusions.

After 1.04 rev, the mass flow in each case gradually decreased to the lowest state. After a period of time, the flow begins to partially recover, and at the same time, typical stall cells also begin to form. As mentioned in Sect. 3, the order of time when the flow begins to recover and enters into stall state is CO-1.0 RID < CO-0.5 RID < UNI < CO-0.0 RID. This phenomenon will be explained based on physical evidence.

Conducting flow analysis based on entropy distribution results. As shown in Fig. 17. It can be seen that there is a clear boundary between the low-entropy region and the high-entropy region around the blade in the rotor domain, and the boundary between the two is also the boundary between main flow and blocked flow. In addition, it is also known from Fig. 17 that the high-entropy region at the inlet corresponds to the low total pressure distortion region and the low-entropy region corresponds to the high total pressure region. Therefore, flow changes will be analyzed based on entropy distribution. When the low-entropy region (blue area) enters the blade channel, it indicates that the blade channel exits the blocked state.
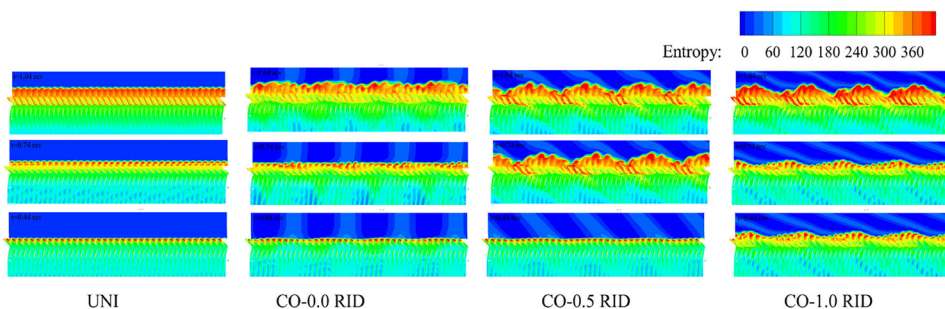
The variations in pressure at blade tip vs outlet mass flow of the four cases are shown in Fig. 18. When the mass flow is at its lowest state, there is also disturbance in the compressor, and the rotational speed of which is basically the same as the speed of the subsequent stall cells. It is not until the mass flow begins to recover that the amplitude of such disturbances begins to increase. This is also consistent with the conclusion of Sect. 3.

When the mass flow is at its lowest state, the S1 flow fields of CO-0.0 RID are shown in Fig. 19. When the protrusions pass through the high-entropy region (low total pressure region) at the inlet, they will spread upstream, which means

Fig. 15 Flow field at 98% span for different cases

(a) initial field

(b) CO-0.0 RID

(c) CO-0.5 RID

(d) CO-1.0 RID
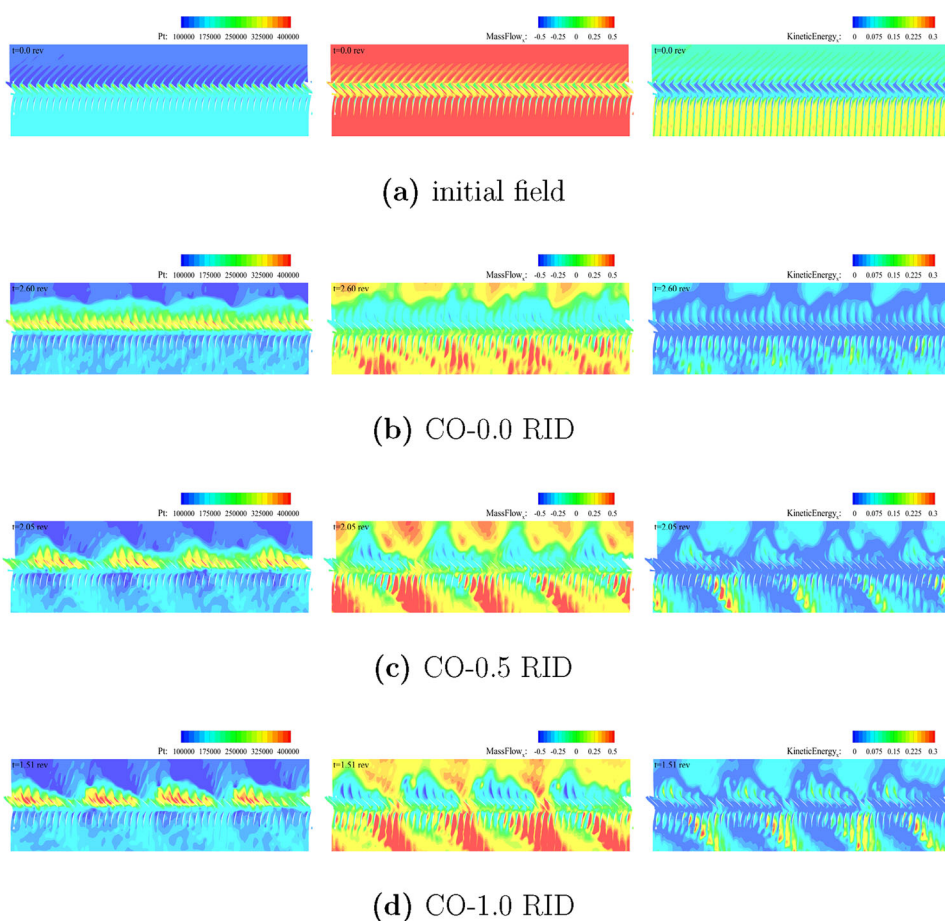
Fig. 16 Entropy distribution at 98% span from 0.44 to 1.04 rev

UNI   CO-0.0 RID   CO-0.5 RID   CO-1.0 RID

they are excited; when the protrusions enter the low-entropy region (high total pressure region), they will retreat downstream, which means they are suppressed. The concaves are also excited periodically by distorted regions with lower total pressure. In this way, the concaves cannot be close to the leading edge of the rotor. This may be why the CO-0.0 RID delays the occurrence of the rotating stall.

The phenomenon of block flow being periodically excited and suppressed is also reflected in variations of mass flow. Observing the mass flow variations of different cases, the following conclusions can be drawn:

1. The fluctuation amplitude of inlet mass flow is greater than that of outlet mass flow.
2. The mass flow fluctuations of CO-0.0 RID and CO-1.0 RID are significant; the mass flow of UNI and CO-0.5 RID has almost no fluctuations.

It can be inferred that the mass flow fluctuation mainly comes from the fluctuation of flow state near the inlet; the fluctuation of flow state is caused by the mutual interference between block flow and distortion disturbance. For UNI, there is no mutual interference; for CO-0.5 RID, the rotational speeds of the two are basically the same and there is almost no mutual interference. The following will analyze
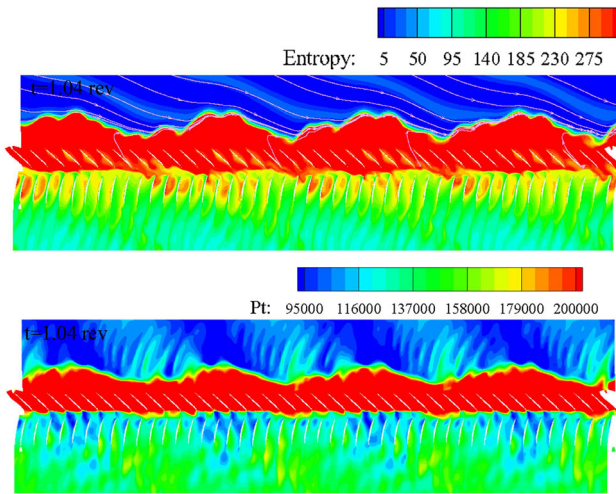
Fig. 17 Streamlines and total pressure at 98% span ($t = 1.04$ rev)

this phenomenon based on theoretical derivation and physical evidence.

Assuming the frequency of the four protrusions is ω_1, the frequency of the four distortion regions is ω_2, and the frequency of their mutual interference is ω. The time interval between the overlap of the protrusions and distorted regions and the next overlap is T. There are the following relationships:

$$T = \frac{2\pi/4}{|\omega_1 - \omega_2|}$$
$$T = \frac{2\pi}{\omega}. \tag{7}$$

It can be calculated that

$$\omega = 4 \cdot |\omega_1 - \omega_2|. \tag{8}$$

It can be seen from Sect. 3 that $\omega_1 = 0.5484$ times of rotor frequency.

First, analyze the change in inlet mass flow for CO-0.0 RID. The peak points and peak separations are shown in Fig. 20. It is evident that the variation in peak separations is relatively small, providing a foundation for averaging. The averaged separation between peaks is 0.452 rev, and the frequency of mass flow fluctuation is $\omega = 1/0.452 = 2.212$ times the rotor frequency. For CO-0.0 RID, $\omega_2 = 0$, the calculated frequency is $4 \cdot |\omega_1 - \omega_2| = 2.194$. The frequency deviation obtained from the calculation and flow analysis is 0.8%, which is very close.

The results of CO-1.0 RID are shown in Fig. 21. The average separation between peaks is 0.553 rev, and the frequency of mass flow fluctuation is: $\omega = 1/0.553 = 1.808$ times the

Fig. 18 Variations in pressure at blade tip vs outlet mass flow

(a) UNI

(b) CO-0.0 RID

(c) CO-0.5 RID

(d) CO-1.0 RID
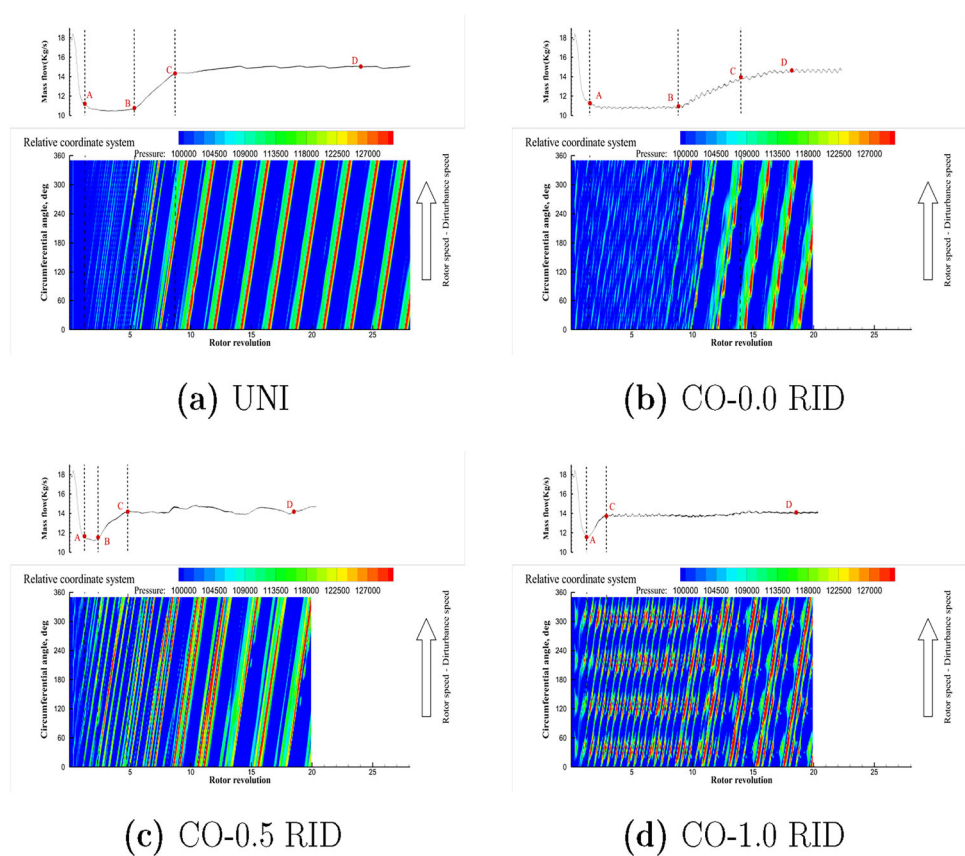
rotor frequency. For CO-0.0 RID, ω_2 is the same as rotor frequency, the calculated frequency is $4 \cdot |\omega_1 - \omega_2| = 1.788$. The frequency deviation obtained from the calculation and flow analysis is 1.1%, which is very close.

The above analysis proves that there is mutual interference between RID and protrusions, and the protrusions are periodically excited and suppressed.

The flow field at 98% span of CO-1.0 RID at 1.11 rev and 1.32 rev is shown in Fig. 22. The rotational speeds of RID and rotor blades are the same, faster than the speed of blocked flow. Under the influence of RID, the blocked area forms four protrusions, corresponding to four concaves. The part enclosed by the black circle in the large image has been enlarged, and the enlarged result is placed in the small image immediately to its right. All black dashed lines in Fig. 22 are located in the same axial position. When the low-entropy region (high total pressure region) sweeps through the concave, compared to the situation where the high-entropy region (low total pressure region) sweeps through, the concaves will move downstream.

The high total pressure regions and rotors have the same rotational speed. When the high total pressure regions sweeps through the concaves, the concaves move downstream, indicating that the boundary between the mainstream and blocked flow moves downstream. As shown in Fig. 23, when this boundary moves downstream to the leading edge line of the rotor(marked with a black dashed line), the corresponding blade channel begins to partially restore normal flow, thus restoring work ability, further causing the boundary to move further downstream. At this point, the mass flow begins to rise and stall cells begin to form.

For CO-0.5 RID, the rotational speed of the distortion regions is very close to the speed of the blocked flow, and there is almost no relative movement between the two. In addition to the small fluctuation of the inlet mass flow mentioned above, this conclusion can also be drawn from Fig. 24.

However, the high total pressure region continues to affect the concave, causing it to eventually retreat to the leading edge of the rotor, as shown in Fig. 25.

For UNI case, there is no effect of incoming flow distortion, and circumferential asymmetry can only occur through the spontaneous disturbance of the flow. Without the influence of external interference, the concaves develops slowly and eventually enters the leading edge line of the rotor, inducing the formation of the stall cell, as shown in Fig. 26.

For CO-0.5 RID and CO-1.0 RID, under the influence of inlet disturbance rotating in the same direction as the rotor, the protrusions are larger and the concaves are also deeper. The concaves are easier to enter the leading edge of the rotor. For CO-0.0 RID, the protrusions and concaves are periodically excited and suppressed, entering into a relatively stable state, resulting in the late appearance of large concaves near the rotor leading edge and the late formation of stall cells.
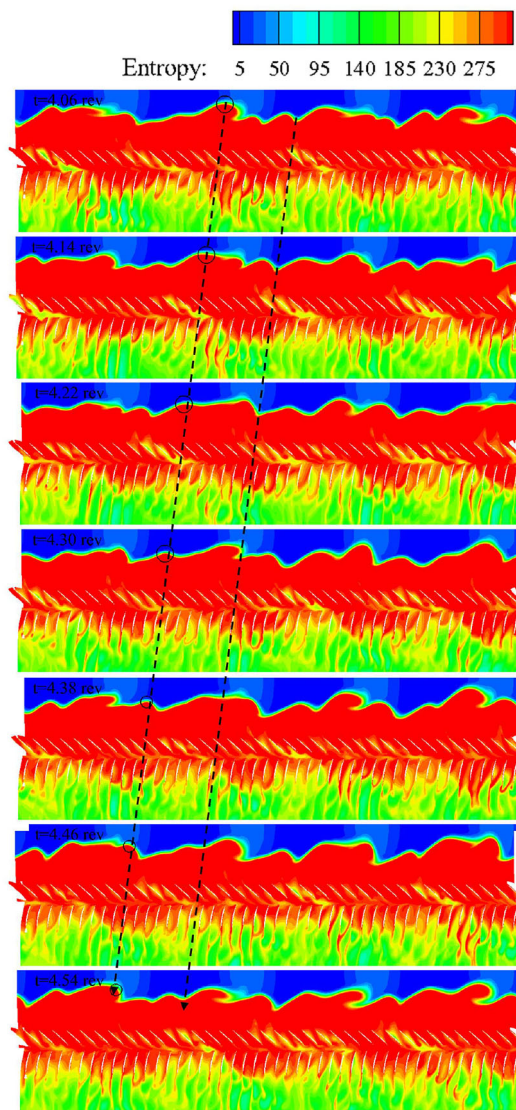

Fig. 19 Entropy distribution of CO-0.0 RID ($t = 4.06$–4.54 rev)

## 4.3 Influence of Distortion on the Formation and Transition of Different Stall States

The variation of flow structure in the CO-0.5 RID case is chosen, as the development process of stall states in the CO-0.5 RID case is more complete than that in the CO-1.0 RID case. The flow field connected to mass flow for the CO-0.5 RID case is shown in Fig. 27.

After the flow is throttled, 4 uniform protrusions are formed, which is marked as state 0. The protrusions are transformed into 4 independent stall groups with the growth process of mass flow, which is marked as stall state 1.
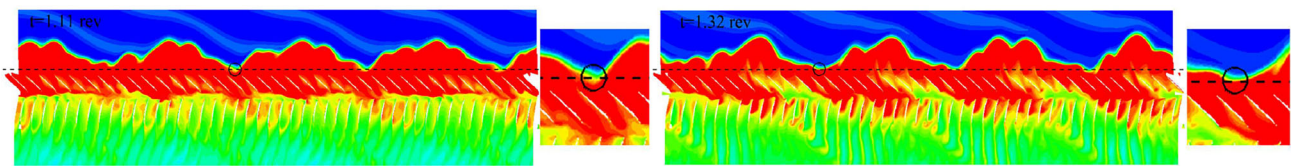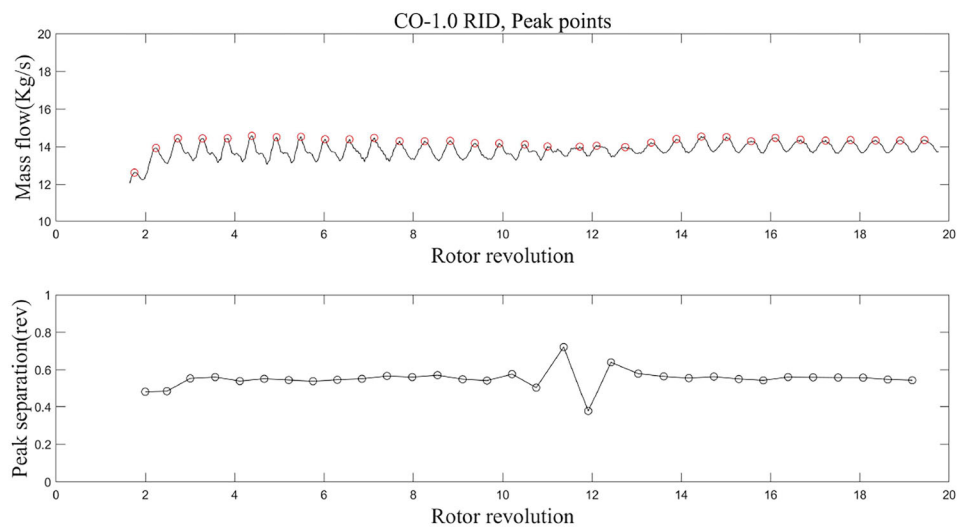
The similarity of the 4 stall groups gradually disappears, then stall state 2 emerged, and the mass flow increases slightly indicating that the flow capacity of the compressor is further improved, which also happens in the CO-1.0 RID case, as
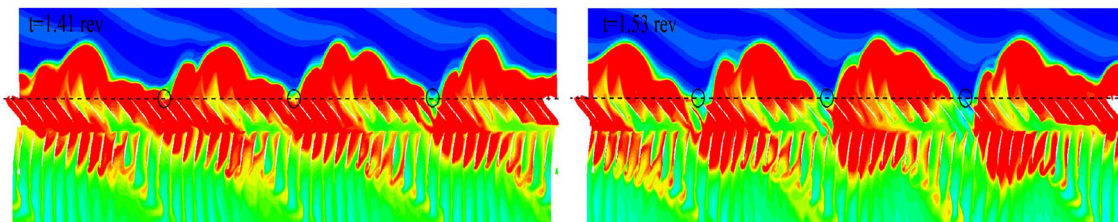
Fig. 20 Peak points of inlet mass flow of CO-0.0 RID
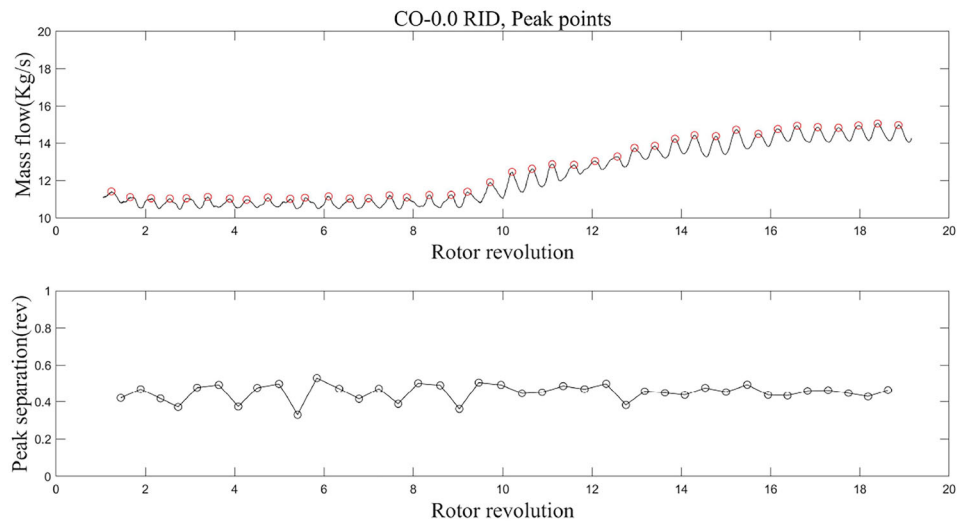
Fig. 21 Peak points of inlet mass flow of CO-1.0 RID

Fig. 22 Entropy distribution of CO-1.0 RID ($t = 1.11$ rev and 1.32 rev)

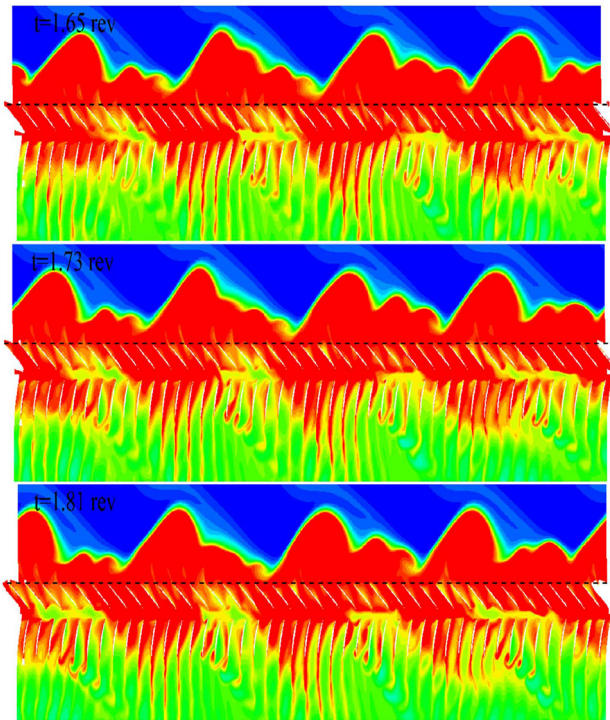**Fig. 23** Entropy distribution of CO-1.0 RID ($t = 1.41$ rev and 1.53 rev)

Fig. 24 Entropy distribution of CO-0.5 RID

Fig. 25 Entropy distribution of CO-0.5 RID

shown in Fig. 10. The stall groups are weakened or enhanced. Finally, one big stall group is formed, which is similar to the big stall group in the UNI case, as shown in Fig. 14.

The flow field when $t = 6.34$ rev is chosen for analysis of the transition from stall state 1 to stall state 2, as marked by the dashed ellipse in Fig. 27.

The installation angle for the rotor blade at 98% span is calculated by connecting the leading point and trailing point, as shown in Fig. 28. The installation angle is expressed with β_k. The flow angle is expressed with β, and the incidence is calculated as Eq. (9) and Fig. 28. It needs to be mentioned that, the incidence makes no sense in the stator region, as the installation angle is calculated based on the rotor blade.

$$
\begin{aligned}
\text{Incidence} &= \beta_k - \beta \\
\beta_k &= 13.1722 \text{ deg} \\
\tan(\beta) &= \frac{U_x}{U_{\theta\_\text{rel}}}.
\end{aligned}
\tag{9}
$$

The flow field at 98% span for CO-0.5 case when $t = 6.34$ rev is shown in Fig. 29. Two typical stall groups are chosen for analysis as marked by the dashed box in the picture at top of Fig. 29. The left one of the stall groups is enhanced, the right one is weakened. The incidence distribution is calculated in Fig. 29 to explain the behavior of stall groups, the total pressure distribution, the axial mass flow distribution, and the axial kinetic energy distribution are also calculated
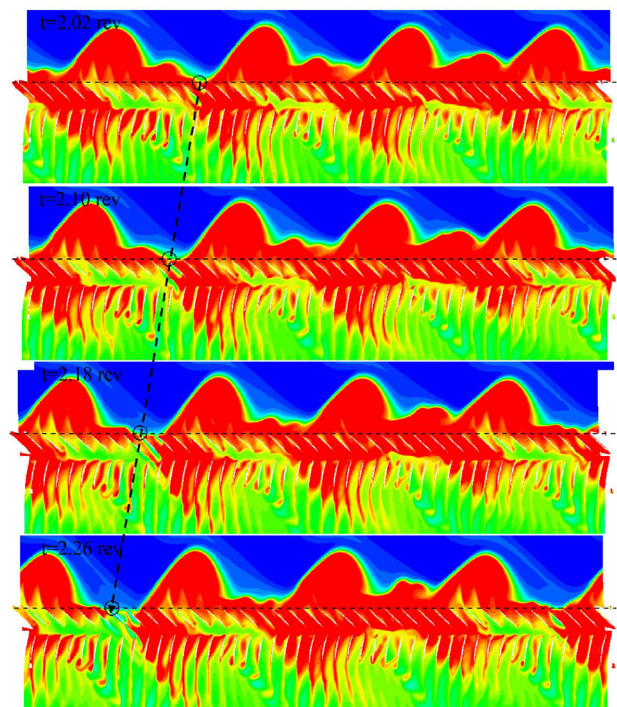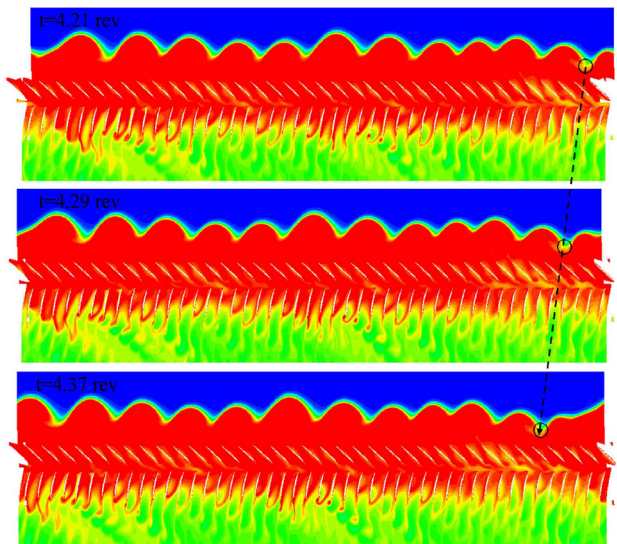

Fig. 26 Entropy distribution of UNI

to explain the distribution of incidence. The left stall group is represented as stall group A, the right stall group is represented as stall group B.

The rotor rotation direction is taken as the positive direction in the following analysis. The blade passage in front of the stall group A is covered by regions with low incidence, which is smaller than that in front of stall group B. What is more, the blade passage behind the stall group A is covered by the high incidence region which is larger than that behind

**Fig. 27** Flow field at 98% span vs mass flow for CO-0.5 RID case
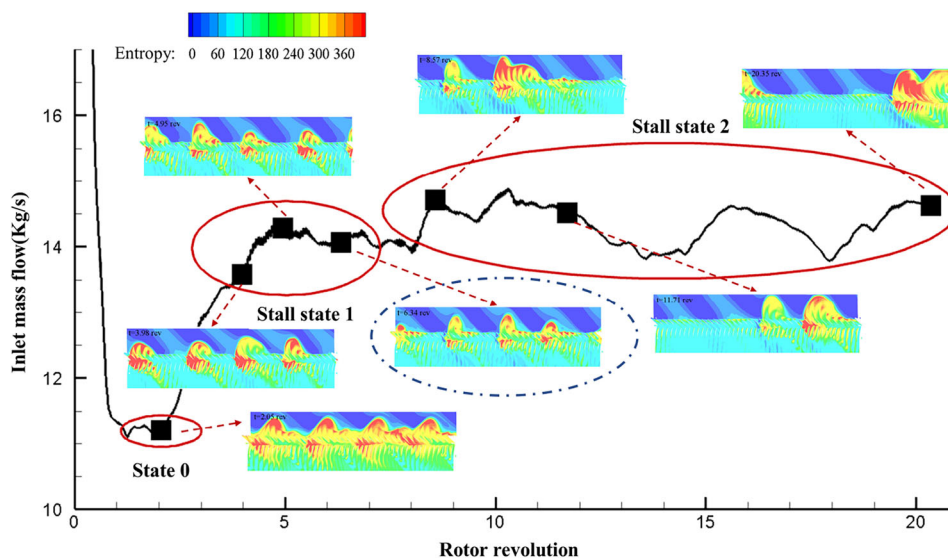
stall group B. It means that, compared with stall group B, stall group A is less weakened in the blade passage in front of itself and more enhanced in the blade passage behind itself. This is why stall group A is enhanced but stall group B is weakened.

It can be seen from the total pressure distribution that, the flow on the right of stall group B is experiencing the distorted region with lower total pressure, and the flow on the left of which is experiencing the distorted region with higher total pressure. The flow in the distorted regions with higher total pressure has larger axial mass flow and higher kinetic energy. Larger axial mass flow is connected with lower incidence, which will enhance the effect for the blade passage in front of the stall group to exit stall status. However, the flow in the distorted regions with lower total pressure will also enhance the effect for the blade passage behind the stall group to enter into stall status.

It is observed that the shape of the stall group also has an influence on the distribution of incidence near rotor blades. Behind stall group B, there also exists a region with higher axial mass flow and lower incidence near the leading edge of the rotor blade, which is induced by the outline of the stall group. Whether it is stall group A or stall group B, near the right boundary of which, there exists flow acceleration. The difference is that, for stall group B, the flow acceleration region is much closer to the rotor blade, which separates the blade passage with higher incidence from the main region of stall group B, thus stall group B is weakened.

It is concluded that, under the combined action of distortion region and outline of stall group, the smaller stall group will be further weakened. As the mass flow at rotating stall status is nearly unchanged, some stall groups are weakened, to maintain the mass flow, the other stall groups will be enhanced.
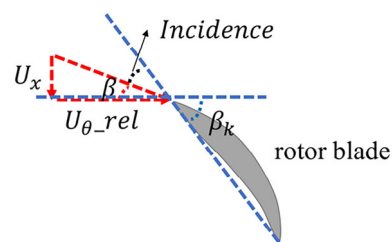
Fig. 28 Calculation of incidence

The possible explanation is that, in stall state 1, some stall groups are weakened due to experiencing the distorted regions with higher total pressure, the size of these stall groups decreases, and the flow acceleration behind them will further weaken itself. It means that stall state 1 is unstable, due to the influence of RID, the stall groups will be weakened or enhanced and only one big stall cell will eventually exist in the current compressor.

Compared with the CO-1.0 case, the rotational speed of RID for the CO-0.5 RID case is closer to the rotational speed of stall groups in state 1, which will have more time to influence the stall groups, thus the state will be destroyed more easily. It is the cause that the transition process occurs earlier in the CO-0.5 RID case than in the CO-1.0 RID case.

5 Conclusions

To study the influence of RID on the development of compressor rotating stall in detail, the stall developments of NASA stage 35 under uniform inlet condition and RID with 4 distorted regions in the whole annulus are simulated. The findings can be summarized as follows:

Fig. 29 Flow field at 98% span for CO-0.5 case when $t = 6.34$ rev
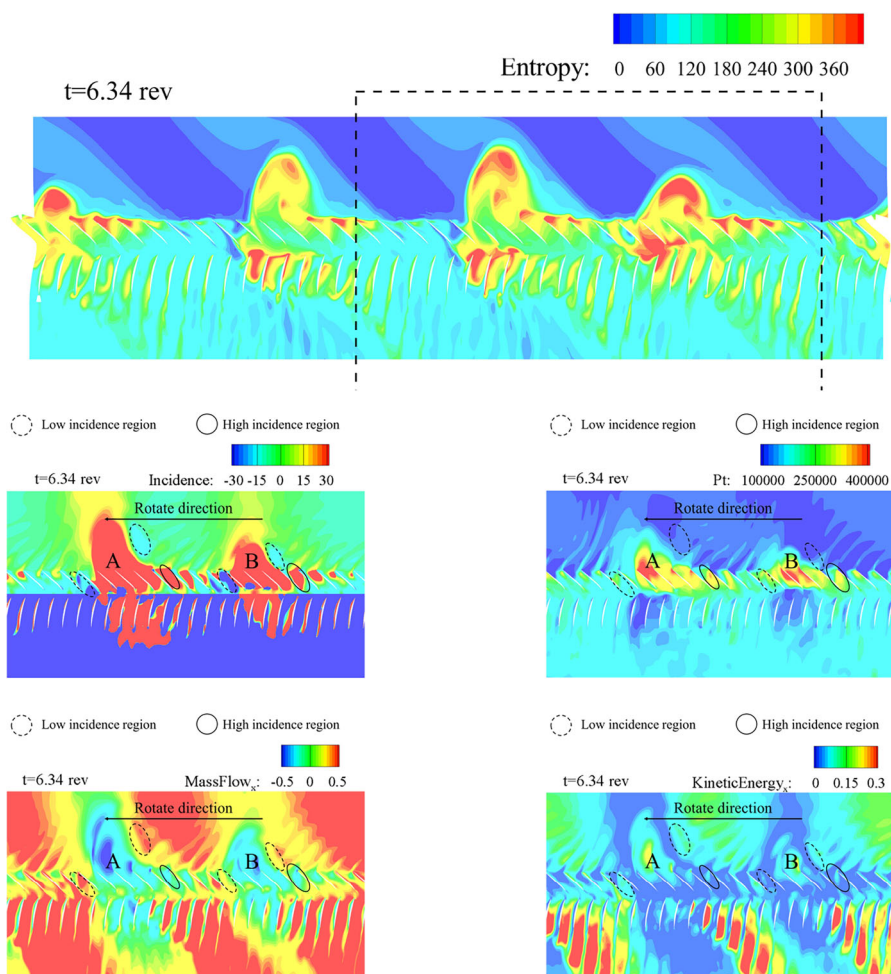
(1) RID has little influence on the rotational frequency and number of stall cells when they are fully developed, which are the inherent characteristics of the compressor.

(2) RID with lower relative rotational speed to rotor will delay the occurrence of rotating stall, RID with higher relative rotational speed will exceed the occurrence of rotating stall but will experience two types of stall states.

(3) For CO-0.5 RID and CO-1.0 RID, under the influence of inlet disturbance rotating in the same direction as the rotor, the protrusions are larger and the concaves are also deeper. The concaves are easier to enter the leading edge of the rotor. For CO-0.0 RID, the protrusions and concaves are periodically excited and suppressed, entering into a relatively stable state, resulting in the late appearance of large concaves near the rotor leading edge and the late formation of stall cells.

(4) Under the RID with 4 distorted regions in the whole annulus, when the relative rotational speed to the rotor is small, 4 independent stall groups will appear with the increase of mass flow, which is marked as stall state 1; then some stall groups are weakened due to experiencing the distorted region with higher total pressure, the volume of these stall groups decreases, the flow acceleration behind which will further weaken itself. It means that, stall state 1 is unstable, due to the influence of RID, the stall groups will be weakened or enhanced and only one big stall cell will eventually exist in the current compressor. The closer the rotational speed of RID is to the stall groups, the transition process from stall state 1 to the final stall state occurs earlier.

This research's findings can help understand the instability behavior of downstream compressor in multi-spool engines, including stall development and stall state transition, under the distortion flow induced by the upstream compressor.

In future work, simulations will be performed in exploring the methods for suppressing the occurrence of rotating stall under RID.

Data Availability Statement The data that support the findings of this study are available from the corresponding author upon reasonable request.

Declarations

Conflict of interest On behalf of all authors, the corresponding author states that there is no conflict of interest.

References

1. Li J, Dong X, Sun D, Xu R, Sun X (2021) Response and stabilization of a two-stage axial flow compressor restricted by rotating inlet distortion. Chin J Aeronaut 34(9):72–82. https://doi.org/10.1016/j.cja.2021.02.005

2. Lee K-B, Wilson M, Vahdati M (2018) Effects of inlet disturbances on fan stability. J Eng Gas Turbines Power 141(5):051014. https://doi.org/10.1115/1.4042204

3. Longley JP, Shin H-W, Plumley RE, Silkowski PD, Day IJ, Greitzer EM, Tan CS, Wisler DC (1996) Effects of rotating inlet distortion on multistage compressor stability. J Turbomach 118(2):181–188. https://asmedigitalcollection.asme.org/turbomachinery/article-pdf/118/2/181/5501129/181_1.pdf. https://doi.org/10.1115/1.2836624

4. Ludwig GR, Arendt RH, Nenni JP (1973) Investigation of rotating stall in axial flow compressors and the development of a prototype stall control system, Usaf-apl-tr-73-45 edn. USAF

5. Peters T, Fottner L (2002) Effects of co- and counter-rotating inlet distortions on a 5-stage HP-compressor. Turbo expo: power for land, sea, and air, vol 5: Turbo Expo 2002, Parts A and B, pp 659–666. https://doi.org/10.1115/GT2002-30395

6. Nie C, Zhang J, Tong Z, Zhang H (2006) The response of a low speed compressor on rotating inlet distortion. J Therm Sci 15:314–318. https://doi.org/10.1007/s11630-006-0314-2

7. Zhang J, Lin F, Chen J, Nie C (2007) Effects of rotating inlet distortion on flow stability of an axial compressor. https://doi.org/10.2514/6.2007-5062

8. Yan W, Hu J, Zhang H, Mao Z, Yin C, Zhang C (2014) Effects of complicated rotating inlet distortion on compressor aerodynamic stability. https://doi.org/10.2514/6.2014-3732

9. Zhang M, Hou A (2015) Investigation on stall inception of axial compressor under inlet rotating distortion. Proc Inst Mech Eng Part C J Mech Eng Sci. https://doi.org/10.1177/0954406215623978

10. Zhang W, Stapelfeldt S, Vahdati M (2020) Influence of the inlet distortion on fan stall margin at different rotational speeds. Aerosp Sci Technol 98:105668. https://doi.org/10.1016/j.ast.2019.105668

11. Moore RD, Reid L (1978) Performance of single-stage axial-flow transonic compressor with rotor and stator aspect ratios of 1.19 and 1.26 respectively, and with design pressure ratio of 2.05, Nasa technical paper 1659 edn. NASA Lewis Research Center, Cleveland

12. Weigl HJ, Paduano JD, Fréchette LG, Epstein AH, Greitzer EM, Bright MM, Strazisar AJ (1997) Active stabilization of rotating stall and surge in a transonic single stage axial compressor. Turbo expo: power for land, sea, and air, vol 4: manufacturing materials and metallurgy; ceramics; structures and dynamics; controls, diagnostics and instrumentation; education; IGTI Scholar Award. V004T15A034. https://doi.org/10.1115/97-GT-411

13. Bright MM, Qammar HK, Wang L (1998) Investigation of pre-stall mode and pip inception in high speed compressors through the use of correlation integral. Turbo expo: power for land, sea, and air, vol 1: turbomachinery. V001T01A092. https://doi.org/10.1115/98-GT-365

14. Chen J-P, Hathaway MD, Herrick GP (2008) Prestall behavior of a transonic axial compressor stage via time-accurate numerical simulation. J Turbomach **130**(4):041014. https://asmedigitalcollection.asme.org/turbomachinery/article-pdf/130/4/041014/5943428/041014_1.pdf. https://doi.org/10.1115/1.2812968

15. Gan J, Im H, Zha G (2015) Simulation of stall inception of a high speed axial compressor with rotor-stator interaction. In: 51st AIAA/SAE/ASEE joint propulsion conference. https://doi.org/10.2514/6.2015-3932

16. Wang Z, Fan Z, Liu F, Jiang X, Li B, Qiu M (2022) Large-scale parallel simulation with implicit conservative overlapped grid technique for compressor flow. Comput Fluids 238:105375. https://doi.org/10.1016/j.compfluid.2022.105375

17. Herrick G, Hathaway M (2009) Unsteady full annulus simulations of a transonic axial compressor stage. https://doi.org/10.2514/6.2009-1059

18. Erdos JI, Alzner E, Mcnally W (1976) Numerical solution of periodic transonic flow through a fan stage. AIAA J 15(11):1559–1568. https://doi.org/10.2514/3.60823

19. Dong X, Sun D, Li F, Jin D, Gui X, Sun X (2015) Effects of rotating inlet distortion on compressor stability with stall precursor-suppressed casing treatment. J Fluids Eng **137**(11):111101. https://asmedigitalcollection.asme.org/fluidsengineering/article-pdf/137/11/111101/6194064/fe_137_11_111101.pdf. https://doi.org/10.1115/1.4030492